UNIVERSITY OF CALIFORNIA,
IRVINE

Molecular dynamics of nanodroplet impact: the effect of molecular models.

THESIS

submitted in partial satisfaction of the requirements
for the degree of

MASTER OF SCIENCE

in Mechanical and Aerospace Engineering

by

Efren Villanueva Bonay

Thesis Committee:
Professor Manuel Gamero-Castaño, Chair
Professor Tim Rupert
Professor Roger H. Rangel

2018

TABLE OF CONTENTS

Page

LIST OF FIGURES **iv**

LIST OF TABLES **vi**

NOMENCLATURE **vii**

ACKNOWLEDGMENTS **ix**

ABSTRACT OF THE THESIS **x**

1 Introduction **1**
- 1.1 Motivation . . . 1
- 1.2 Theoretical and computational overview . . . 4
  - 1.2.1 Properties of the Silicon slab . . . 4
  - 1.2.2 Molecular Dynamics . . . 6
  - 1.2.3 Interatomic potentials . . . 9
  - 1.2.4 Statisticals Mechanics . . . 14
- 1.3 Literature review . . . 17
- 1.4 Objectives . . . 24
- 1.5 Thesis Overview . . . 25

2 Simulation Methods **26**
- 2.1 Simulation setup . . . 26
- 2.2 Silicon target . . . 27
- 2.3 Nanodroplet models . . . 27
- 2.4 Interactive potentials . . . 28
- 2.5 Nanodroplet parameters . . . 30

3 Results **32**
- 3.1 Temperature field . . . 32
- 3.2 Energy transfer . . . 34
- 3.3 Collision crater . . . 37
- 3.4 Sputtering . . . 39
- 3.5 Amorphization. Coordination number . . . 41
- 3.6 AM model broken bonds . . . 42

3.7 Strong-bond AM model 43

4 Conclusion **46**
4.1 Summary 46
4.2 Recommendations for Future Work 48

Bibliography **49**

LIST OF FIGURES

Page

1.1 Silicon cubic diamond cell with a lattice parameter a = 5.431. 5
1.2 SW potential function which vanishes for r = 1.8. 10
1.3 ZBL screeninig function where the its argument x is defined as the distance scaled with the universal reduced coordinate a 12
1.4 Morse potential function. 13
1.5 Particles contained in the spherical shell between r and $r + dr$ of the control volume. 15
1.6 Radial distribution function for the Argon in solid, liquid and gas phases. . . 16
1.7 Amorphous thickness ratio to the droplet diameter vs kinetic energy for different projectile diameters. 22
1.8 Volume of the amorphous Silicon region vs kinetic energy for different projectile diameters. 23

2.1 Connection of the ZBL and Morse potentials by means of an interpolation spline for the C-H bond in the Formamide molecule. 29

3.1 Cross sectional temperature map view of the four models collisions at $t/t_c = 1$, with velocities of 5 km/s for the EMIMIm and 5.818 km/s for the formamide. (a) Formamide PA model; (b) Formamide AM model; (c) EMIMIm PA model; (d) EMIMIm AM model. 33
3.2 Evolution in time of the (a) droplet kinetic energy and (b) potential, (c) thermal, (d) translational target energies for the EMIMIm and formamide PA and AM models for a droplet initial kinetic energy of 15.31 KeV. 35
3.3 Average layer temperature for the four models simulated at the highest droplet initial kinetic energy. (a) Formamide PA model at 8.145 km/s; (b) Formamide AM model at 8.145 km/s; (c) EMIMIm PA model at 7 km/s; (d) EMIMIm AM model at 7 km/s. 36
3.4 4 EMIMIm collision of the projectile for the PA model and AM model at velocities 5 km/s and 7 km/s and for $t/t_c = 4$ and $t/t_c = 8$. (a) PA at 5 km/s for $t/t_c = 4$; (b) PA at 5 km/s for $t/t_c = 8$; (c) PA at 7 km/s for $t/t_c = 4$; (d) PA at 7 km/s for $t/t_c = 8$; (e) AM at 5 km/s for $t/t_c = 4$; (f) AM at 5 km/s for $t/t_c = 8$; (g) AM at 7 km/s for $t/t_c = 4$; (h) AM at 7 km/s for $t/t_c = 8$. . 38
3.5 Craters left after 100 ps of simulation for the AM and PA models for the five different droplet initial kinetic energies. 38

3.6 Coordination number field after 100 ps of simulation for the four models at the highest droplet kinetic energy. (a) Formamide PA model at 8.145 km/s; (b) Formamide AM model at 8.145 km/s; (c) EMIMIm PA model at 7 km/s; (d) EMIMIm AM model at 7 km/s. 40
3.7 Amorphous Silicon phase depth in function of initial droplet kinetic energy for the four different models. 41
3.8 Broken bonds ratio for the formamide (a) and EMIMIm (b) AM droplet models for different projectile initial kinetic energies 43
3.9 Comparison of the kinetic droplet energy and thermal, translational and potential target energies between the EMIMIm AM model and the EMIMIm AM model with strong bonds for a velocity of 7 km/s. 44
3.10 Coordination number field after 100 ps for the EMIMIm AM model with unbreakable bonds for a velocity of 7 km/s. 45

LIST OF TABLES

Page

2.1 Formamide and EMIMIm liquid molecule parameters. 28
2.2 Formamide Morse potential parameters. 30
2.3 EMIMIm Morse potential parameters. 30
2.4 Droplet kinetic energy and corresponding velocities and characteristic times for the two molecule types. 31

3.1 Number of sputtered Si atoms for the PA and AM EMIMIm and formamide models at the five initial droplet kinetic. 39

NOMENCLATURE

Roman Symbols

$\mathbf{f}$	Force vector
$\mathbf{r}$	Position vector
$\mathbf{v}$	Velocity vector
$\mathbf{x}$	Particle coordinates
D	Diameter
D_e	Dissociation energy
E_k	Kinetic energy
E_P	Potential energy
E_{CM}	Translational energy
E_{Th}	Thermal energy
$g(r)$	Radial distribution function
K_B	Boltzman constant
k_e	Spring constant of an harmonic potential function
m	Mass
N	Number of particles in the system
r	Radial location
r_0	Bond equilibrium distance
T	Temperature
t	Time
t^*	Dimensionless time
t_c	Characteristic time

U	Potential energy
x, y, z	Cartesian coordinate system
Z	Atomic number

Greek Symbols

ϵ_0	Vaccum permittivity
Φ	Potential energy function
σ	Cutoff radius
θ	Dihedral angle
ρ	Density

Subscripts

i	i-th particle property

Acronyms

AM	Atomic/Molecule model
CN	Coordination Number
EAN	ethanaminium nitrate
EMIMIm	1-ethyl-3-methylimidazolium bis (trifluoro-methylsulfonyl) imide
HPC	High Performance Computing
MD	Molecular Dynamics
NVE	System isolated from changes in moles(N), volume(N) and energy(E)
PA	Pseudo-Atom model
SW	Stillinger-Weber potential function
ZBL	Ziegler-Biersack-Littmark potential function

Superscripts

N	All N particles property

ACKNOWLEDGMENTS

First of all, I would like to express my gratitude to my advisor Professor Manuel Gamero-Castaño, for his unconditional support, patience and his invaluable guidance through my work.

I would also like to sincerely thank Pete Balsells, founder of the Balsells Fellowship program, and its director Professor Roger Rangel. They have given me the opportunity to study at the University of California, Irvine. It has helped me to grow both academically and personally.

I must also thank my parents and friends for their continuous support.

ABSTRACT OF THE THESIS

Molecular dynamics of nanodroplet impact: the effect of molecular models.

By

Efren Villanueva Bonay

Master of Science in Mechanical and Aerospace Engineering

University of California, Irvine, 2018

Professor Manuel Gamero-Castaño, Chair

Electrospraying of nanodroplets modifies the target surface by sputtering its atoms and amorphizing the outer layers. Collisions of droplets of diameters between 1 nm and 1 μm are not yet totally understood. Previous experimental studies have been performed and compared with Molecular Dynamics simulations using the pseudo-atom model (PA) for the droplets. This PA model considers each liquid molecule as a single particle with the same molecular mass. In this study a new atomic/molecule model (AM) which contemplates all atoms and bonds of the droplet is presented. Simulations of the collision of a 5 nm diameter droplet for formamide and EMIMIm are performed using both models. Droplet initial kinetic energies between 3 KeV and 15 KeV are tested. Results show that PA model collisions transfer almost all of their initial kinetic energy to the slab. Temperature fields after the collision are much higher for this model. Furthermore, highly energetic EMIMIm droplets pseudo-atoms penetrate further into the target whereas atoms in the AM model do not. The ratio of Silicon atoms sputtered and the amorphized region depth for the PA models are larger than for the atomic/molecule, which compare well to experimental results. The AM model is more accurate, especially when simulating droplets of high atomic mass for which the PA model particles are very energetic. Energy consumed to break bonds in the AM model is negligible in comparison with the droplet initial kinetic energy. Simulations show that unbreakable bonds can be used in the AM models obtaining almost identical results.

Chapter 1

Introduction

1.1 Motivation

The energetic impact of electrosprayed nanodroplets on hard surfaces modifies the target in different ways. They amorphize outer atoms of the surface after being melted due to the droplet impact; they leave craters of depth comparable to the projectile size; and, at high enough kinetic energies, they can sputter a large number of atoms.[1,2] Nanoprojectiles do not penetrate deep into the target but quickly transmit their energy to the surface. The impact of light particles at atomic level have been widely studied on basis of Sigmund's collision cascade model.[3] Larger projectiles of 1 μm or more have been also considered in detail.[4,5] However, the remaining range is not yet totally understood.

Silicon is an extensively used material due to its low cost and high industrial applications because of its semiconductivity. It is used in many electronic devices and photovoltaic panels.[6,7] Amorphous Silicon has a higher conductivy and, therefore, manufacturing ways to obtain it have been widely studied. The electrospraying of highly energetic nanodroplets

at hypervelocities amorphizes Silicon surfaces around the region of the impact. This amorphization is in part achieved by the sputtering of Si atoms from the surface.[1]

Molecular Dynamics simulations are used in this study to further investigate what happens during and after the impact of these nanodroplets. Molecular Dynamics is a powerful technique employed to obtain accurately position and velocity of all particles inside a simulation cell. It integrates the equations of motion at every step of the simulation. The forces between particles are obtained from different interacting potentials. It allows the computation of thermodynamic properties such as temperature, pressure or density as well as other parameters like the radial distribution function which gives information about the target structural phase.

Sputtering and amorphization of the collided Silicon slabs have been analyzed in previous studies experimentally[8,2] and by Molecular Dynamics simulations.[9,10] However, previous simulations have used the pseudo-atom model (PA) in which the molecules of the droplet are represented by particles with same molecular mass. This model can miss several key aspects of the impact since it does not take into account the molecular composition of the projectile and the intramolecular interactions.

The present study introduces a new atomic/molecule model (AM) where all atoms in the nanodroplet molecules and their bonds are considered. This model provides a more realistic way to reproduce the impact, sputtering and subsequent amorphization of the target slab. This article presents the comparison of these two models on the simulation of a 5 nm diameter nanodroplet collision into a (100) Si target. Two liquids of distinct molecular masses are considered: formamide and 1-ethyl-3-methylimidazolium bis (trifluoro-methylsulfonyl) imide (also known as EMIMIm). Both have been used in previous studies. In particular, energy transferred into the slab, sputtering rates and depth of the amorphized region are compared

in this article. Furthermore, a study of the AM model broken bonds and the relevance of the energy lost on that process is presented.

1.2 Theoretical and computational overview

This section introduces an overview of different topics which serve as a basis in this study. First of all properties of Silicon are presented followed by a brief explanation on Molecular Dynamics. Then, the three different potentials employed in simulations are introduced. A short definition of the formulae used in the following chapters concludes this overview.

1.2.1 Properties of the Silicon slab

Silicon is the fourteenth chemical element and it belongs to the metalloids. It has an atomic mass of 28.09 u and and a density of 2330 Kg/cm^3 at room temperature. The general structural phases of Silicon are crystalline, amrophous and liquid. In crystalline phase at atmospheric pressure, Si atoms are organized in a cubic diamond cell which contains 8 full Si atoms. The cell has a lattice constat $a = 5.431$Å. In this phase, the coordination number is $CN = 4$ which means that each atom establishes four bonds with its closer neighbours. The melting point is at 1685 K at a pressure of 1 atm. Amorphous Silicon is a solid phase with Si atoms arrenged randomly. It has a coordination number above 4. Finally, liquid Silicon phase is obtained after reaching the melting point and it has a coordination number above 5.[11]

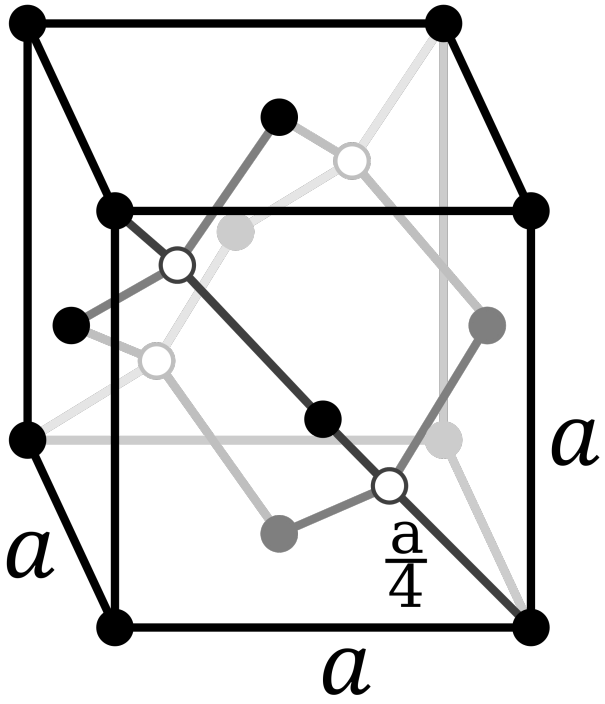

Figure 1.1: Silicon cubic diamond cell with a lattice parameter a = 5.431.

1.2.2 Molecular Dynamics

Molecular Dynamics is a computer simulation technique that provides detailed information of the fluctuations and conformational changes of atoms and molecules. It is used to understand the properties of atoms and molecules in terms of their structure and the microscopic interactions between them. The trajectories of atoms and molecules are computed by numerically integrating Newton's equations of motion where forces and energies are calculated using interatomic potentials.

Typically, molecular systems consist of a large number of particles which makes it impossible to solve the motion equations analytically. For this reason, Molecular Dynamics are employed using numerical methods. However, the simulations are constraint by the available computation power. Parameters such as the number of particles, the timestep and the total simulation duration must be chosen adequately so that the simulation is finished in a reasonable time. Still, the simulated time should be long enough to obtain relevant results of the processes studied.

Simulation results act as exact predictions and are often compared to experimental results. They are exact in the sense that one can make them as accurately as the computation budget allows. It might be necessary to model a test and simulate it before building the experimental setup in order to save time and resources. Moreover, sometimes it is not possible to obtain experimental results in the laboratory because it is difficult or impossible to do so. Furthermore, with MD simulations, data at each timestep is obtained but there might be no recording tools available to do so experimentally.

Numerical simulations consists on the solution of the following system at each timestep:

$$m_i \ddot{\boldsymbol{r}}_{\boldsymbol{i}} = \boldsymbol{f_i} \tag{1.1}$$

$$\boldsymbol{f_i} = -\frac{\partial U}{\partial \boldsymbol{r_i}} \tag{1.2}$$

Forces $\boldsymbol{f_i}$ are needed for each particle. They are obtained deriving the potential energy $U(\boldsymbol{r_i})$, where $\boldsymbol{r^N} = (\boldsymbol{r_1}, \boldsymbol{r_2}, ..., \boldsymbol{r_N})$ are all the space coordinates for each atom.

The interaction potential acting on each particle is defined as the sum of the following contributions:

$$U(\boldsymbol{r_N}) = U_{non-bonded}(\boldsymbol{r_N}) + U_{intramolecular}(\boldsymbol{r_N}) \tag{1.3}$$

The non-bonded contribution is obtained by the interaction potential between particles that are not connected by a bond. It is split into 1-body, 2-body, 3-body... interactions but, usually, only the 1-body and 2-body terms are considered, neglecting the higher order ones:

$$U_{non-bonded}(\boldsymbol{r_N}) = \sum_i u(\boldsymbol{r_i}) + \sum_i \sum_{j>i} v(\boldsymbol{r_i}, \boldsymbol{r_j}) + ... \tag{1.4}$$

Where $u(\boldsymbol{r_i})$ corresponds to the potentials associated to walls or external objects and $v(\boldsymbol{r_i}, \boldsymbol{r_j})$ is the interactomic pair potential between particles.

Finally, the interacting potential between bonded atoms is build up by four terms that account for the energies stored in bonds, angles, dihedrals and impropers.

$$\begin{aligned} U_{intramolecular}(\boldsymbol{r_N}) = &\sum_{i,j} U_{bond}(\boldsymbol{r_i}, \boldsymbol{r_j}) + \sum_{i,j,k} U_{angle}(\boldsymbol{r_i}, \boldsymbol{r_j}, \boldsymbol{r_k}) + \sum_{i,j,k,l} U_{dihedral}(\boldsymbol{r_i}, \boldsymbol{r_j}, \boldsymbol{r_k}, \boldsymbol{r_l}) \\ &+ \sum_{i,j,k,l} U_{improper}(\boldsymbol{r_i}, \boldsymbol{r_j}, \boldsymbol{r_k}, \boldsymbol{r_l}) \end{aligned} \tag{1.5}$$

Once the potential functions are defined, the forces applied at each particle are calculated using the Verlet algorithm.[12] This is a low order algorithm which does not involve storing high derivatives values and allows timesteps to be increased as much as possible. The timestep selection is crucial in the simulation. Having an NVE system where atoms, volume and total energy must remain constant during the whole simulation, a timestep that fulfills this conditions must be selected. In this study, a timestep of 1 fs has been selected following previous works.[13] This value is lower than the inverse of the highest photon frequency for a crystalline Silicon solid.[14]

1.2.3 Interatomic potentials

Each pair of particles need at least to have one potential function defined in order to obtain the force interactions. For this work, a Stillinger-Weber potential function has been used for the Silicon slab. The Ziegler-Biersack-Littmark potential is used to recreate all collisions and a Morse potential to define the bonded atoms of the droplet.

Stillinger-Weber potential

The Stillinger-Weber (SW) potential[15] is a potential function first introduced by Frank H. Stillinger and Thomas A. Weber in 1985. It comprises both two and three body interactions and it is designed to describe Silicon interactions both in solid and liquid phases. This is what makes it an exceptional potential function to reproduce forces between Si atoms in a cubic diamond lattice from low temperatures up to temperatures surpassing the melting point.

The general potential-energy function has the following form:

$$\Phi(1,...,N) = \sum_i \upsilon_1(i) + \sum_{i,j>i} \upsilon_2(i,j) + \sum_{i,j>i,k>j} \upsilon_3(i,j,k) + ... + \upsilon_N(1,...,N) \tag{1.6}$$

Where υ_1 corresponds to the single particle interactions with walls or external forces and interactions higher than υ_3 will be neglected. Thus, the two and three body interaction potentials are defined as:

$$\upsilon_2(r_{ij}) = \epsilon f_2(r_{ij}/\sigma) \tag{1.7}$$

$$\upsilon_3(\boldsymbol{r_i}, \boldsymbol{r_j}, \boldsymbol{r_k}) = \epsilon f_3(\boldsymbol{r_i}/\sigma, \boldsymbol{r_j}/\sigma, \boldsymbol{r_k}/\sigma) \tag{1.8}$$

The f_2 depends only on scalar distances whereas f_3 accounts for translational and rotational energy. A five-parameter potential family is selected for the reduced potentials f_2 and f_3.

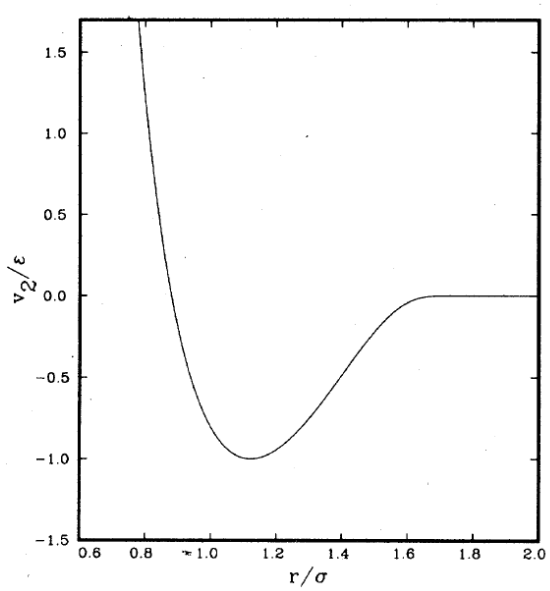

Figure 1.2: SW potential function which vanishes for r = 1.8.

They are applied up until a cutoff $r < a$, after that point the potential vanishes Fig. 1.2.

$$f_2(\boldsymbol{r}) = A(Br^{-p} - r^{-q})exp[(r-a)^{-1}] \tag{1.9}$$

$$f_3(\boldsymbol{r_i}, \boldsymbol{r_j}, \boldsymbol{r_k},) = h(r_{ij}, r_{ik}, \theta_{jik}) + h(r_{ji}, r_{jk}, \theta_{ijk}) + h(r_{ki}, r_{kj}, \theta_{ikj}) \tag{1.10}$$

The function h belongs to a two parameter function:

$$h(r_{ij}, r_{ik}, \theta_{jik}) = \lambda exp[\gamma(r_{ij}-a)^{-1} + \gamma(r_{ik}-a)^{-1}](cos\theta_{jik} + 1/3)^2 \tag{1.11}$$

The most satisfactory values for the seven parameters chosen by Stillinger and Weber were:

$$A = 7.049556277, B = 0.6022245584, p = 4, q = 0, a = 1.8, \lambda = 21.0, \gamma = 1.2 \tag{1.12}$$

Ziegler-Biersack-Littmark potential

The Ziegler-Biersack-Littmark potential or ZBL is a screened Coulomb potential that computes the nuclear repulsion for high energy collisions between atoms. It was first introduced the three authors in the book *The stopping and range of ions in matter*.[16]

The potential function proposed is of the form showed in Eq. 1.13 which contains an screening function $\Phi(r_{ij}/a)$. It is an exponential function (Eq.1.14) and its form is compared to other known screeninig functions in Fig. 1.3. The parameter a in Eq.1.15 is the universal reduced coordinate where a_0 is the Bohr radius $a_0 = 0.529\text{Å}$

$$E_{ij}^{ZBL} = \frac{1}{4\pi\epsilon_0}\frac{Z_i Z_j e^2}{r_{ij}}\Phi(r_{ij}/a) \tag{1.13}$$

$$\Phi(x) = 0.18175e^{-3.19980x} + 0.50986e^{-0.94229x} + 0.28022e^{-0.40290x} + 0.02817e^{-0.20162x} \tag{1.14}$$

$$a = \frac{0.8853a_0}{Z_i^{0.23} + Z_j^{0.23}} \tag{1.15}$$

Z_i and Z_j are the atomic numbers of the pair of atoms, e is the electron charge and ϵ_0 is the vaccum permittivity or electric constant.

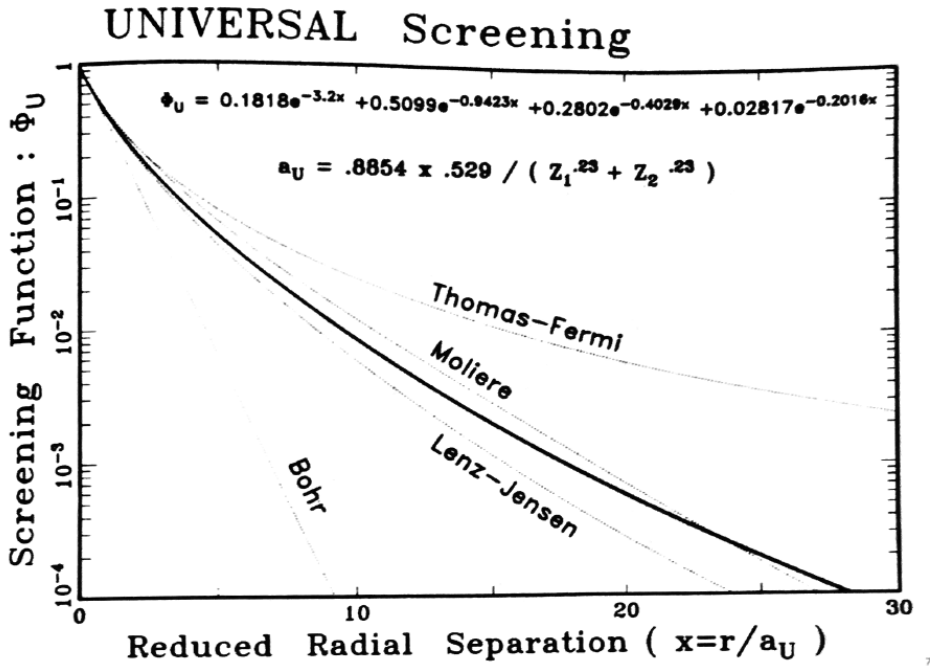

Figure 1.3: ZBL screeninig function where the its argument x is defined as the distance scaled with the universal reduced coordinate a

Morse potential

The Morse potential[17] is named after the physicist Philip M. Morse who proposed it in the year 1929. It is a better approximation than the harmonic potential for a bonded pair of particles because it explicitly includes the effect of bond breaking.

$$U(r_{ij}) = D_e(e^{-2a(r_{ij}-r_0)} - e^{-a(r_{ij}-r_0)}) \tag{1.16}$$

Where r_0 is the bond equilibrium distance and D_e is the dissociation energy which determines the depth of the potential minimum observed in Fig. 1.4. The parameter a is defined as $a = \sqrt{k_e/2D_e}$ where k_e is the spring constant of an harmonic potential function.

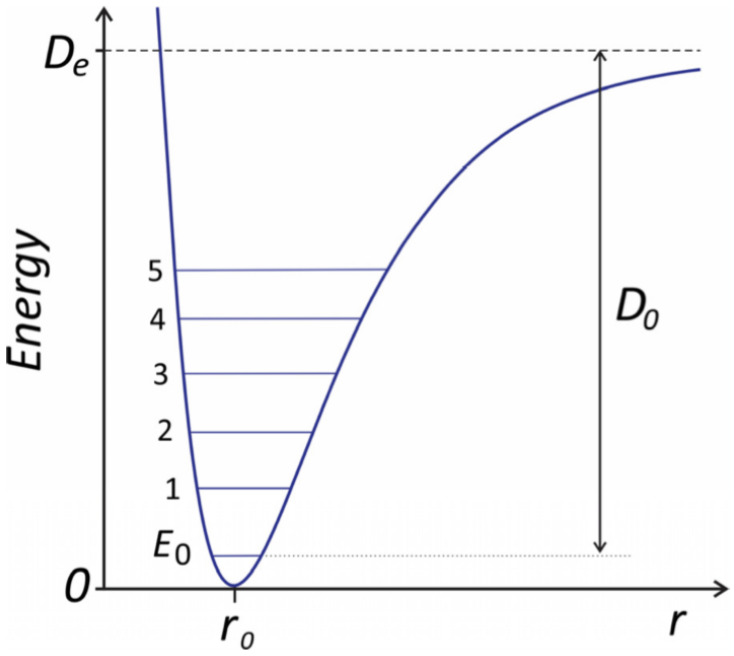

Figure 1.4: Morse potential function.

1.2.4 Statisticals Mechanics

Molecular dynamics simulations produce a huge ammount of data which basically consists in the position and velocity of the millions of particles inside the simulation cell. However, most of the time this is not enough to provide the desired results. For this reason, statistical mechanics are needed to obtain such seeked properties. Statistical mechanics relate the microscopic properties of single particles to the macroscopic ones related to the material.

Temperature

Temperature is computed in terms of the equipartition theorem. This theorem relates the temperature of a system of particles to its average energy. The original idea of the theorem is that, when the equilibrium is reached, the energy is shared equally by all its forms. For example, in thermal equilibrium, the kinetic energy in one degree of freedom in translational motion should be the same than in rotational motion.

The equipartition theorem predicts that the average energy of every degree of freedom is $1/2K_BT$ and therefore contributes to $1/2K_B$ to the system heat capacity. Thus, the average total energy of a system with N particles must be $3/2NK_BT$. The average kinetic energy of a control volume with N particles centered in a particle j is computed as:

$$E_k = \frac{1}{2}\sum_{i}^{N} m_i(\boldsymbol{v}^i - \langle \boldsymbol{v}^j \rangle)^2 \tag{1.17}$$

Where $\langle \boldsymbol{v}^j \rangle$ is the average velocity in the control volume and m_i is the mass of each i-th particle. Therefore, the average temperature of that control volume is computed as:

$$T(\mathbf{x}_j) = \frac{\sum_{i=1}^{N} m_i(v_i - \langle v_j \rangle)^2}{3K_BN} \tag{1.18}$$

Radial distribution function

The radial distribution function is of fundamental importance because it relates microscopic details to macroscopic properties. It is needed to obtain information about the structural phase of the Silicon slab by means of the Coordination Number (CN) computation.

The radial distribution function $g(r)$ describes how density varies with distance from a reference particle. In other words, if $\rho = N/V$ is the number density of the control volume, $\rho g(r)$ is the local particle density at a distance r from the center of it.

The radial distribution function at each point r is computed by determining the average number of particles contained in a spherical shell between r and $r + dr$ from the center of the control volume as showed in Fig. 1.5. Then it is normalized with the number density of the system ρ multiplied by the volume of the spherical shell $4\pi r^2 dr$.

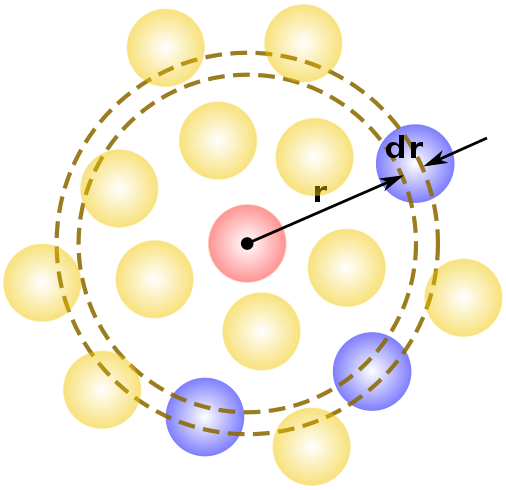

Figure 1.5: Particles contained in the spherical shell between r and $r + dr$ of the control volume.

Fig. 1.6 shows the different forms of the radial distribution function for solid, liquid and gas structural phases of Argon. It is observed how the peaks of the radial distribution function of the solid phase smooth out when the Argon melts and evaporates.

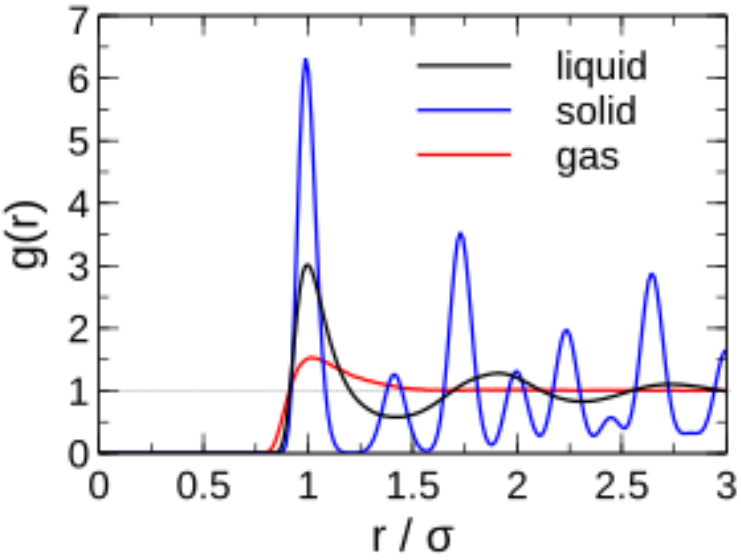

Figure 1.6: Radial distribution function for the Argon in solid, liquid and gas phases.

Coordination number

The coordination number (CN) is used to determine the crystallographic structure of a crystal and its amorphization. The CN of an atom in a moelcule or crystal is the number of neighbouring atoms bonded to it. It can be obtained by integrating the radial distribution function in spherical coordinates up to the first minimum (r') following the Eq.1.19.

$$CN(r') = 4\pi\rho \int_0^{r'} g(r)^2 dr \tag{1.19}$$

For the Silicon, a coordination number of 4 indicates a crystalline Si phase. Around 4.2 the Silicon is considered to be amorphous and for values of 4.6 Silicon it is considered to be in a glassy phase. For CN = 5 and above it is in liquid state.[18]

1.3 Literature review

The following section introduces relevant information and several published journal references that have been essential to establish the basis knowledge of electrospraying amorphization and sputtering studied in this work.

Sputtering

Sputtering is the process of ejecting atoms from a target surface after being collided by energetic projectiles. In order to sputtering to be effective, the kinetic energy of the particles bombarded must be high enough and much higher than conventional thermal energies (1eV).[19,20]

Sputtering is driven by a change of momentum during the projectile collision into the target. When the target particles achieve levels of energy higher than the binding energy that holds them to the surface, atoms leave the target. Sputtering is measured in terms of sputter yield or rate which is the average number of particles ejected divided by the number of particles or ions that the incident projectile has.

The most common type of sputtering is electronic sputtering. It is achieved by energetic electrons or by highly energetic heavy ions that transfer the energy to the target by electronic stopping power.[21]

After a prolonged exposition, sputtering erodes the target surface damaging it, which generally is not desired. However, there are some applications where it may become useful. It is commonly used in thin-film surface deposition, etching and analytical techniques. The film deposition is a type of physical vapor deposition which consists in the deposition of

the sputtered atoms from the target into another material surface, the substrate. It has many useful uses such as solar cells, optical components or semiconductors manufacturing. Analysis techniques such as secondary ion mass spectometry (SIMS) use sputtering to etch away the material while measuring its concentration using mass spectometry.

Amorphization of the Silicon

Amorphous Silicon is a material with huge applications in the industry. It can be achieved by nanoprojectiles electrospraying which has been lately studied because this phenomenona is not observed during macroscopic shock waves.[22] The impact of macroprojectiles leaves the target in a polycrystalline state.[23]

There is a difference between amorphous and glassy Silicon phases. However both are commonly referred as amorphous Silicon. The glassy phase is obtained when Si solidifies at cooling rates that impede recristallization around $10^9 K/s$.[24] On the other hand, the amorphous phase is obtained by other methodes such as milling, indentation, ion irradiation, pressure-induced vitrifcation, etc.[25]

A high velocity droplet impact into a crystalline Silicon target amorphizes a region of comparable volume.[26] This phase transition is mainly due to fast quenching. Droplet particles do no penetrate deep into the surface but generate a collision cascade of knock-on Si atoms that increase their thermal energy resulting in the melting of the collided area. The melted area is quickly cooled down at rates of $10^{14} K/s^2$ which exceeds the recristallization cooling rate preventing the Silicon to recrystallize and therefore solidifying as a glassy region.

Experiments on Silicon sputtering

As stated before, a wide range of macroscopic nanodroplets high energetic impacts have been studied.[27] Moreover, collisions at atomic level have been extensively experimented for a long time.[3] However, a intermediate range of nanometric droplets is yet to be fully understood. Investigations on electrospraying nanodroplets by Fernández de la Mora et al. Ref.[28] improved the understanding of electrospraying and allowed the first experiments on ionic liquid nanodroplets impacts.[29]

Gamero-Castaño and Mahadevan early performed experiments of the bombardment of nanodroplets into single-crystal Silicon and polycrystalline Si. Sputtering yields between 1.5 and 2.5 were obtained for molecule kinetic energies ranging between 24.1 eV and 91.2 eV. Furthermore, Borrajo-Pelaez et al. Ref.[1] experimented with single-crystals semiconductors of Si, SiC, InAs, InP, Ge, GaAs, GaSb, and GaN obtaining sputtering rates between 1.9 for SiC and 4.5 for Ge. The case of Silicon was further analyzed. They pointed out that the consecutive nanodroplet impacts damage the Si surface and leave craters that play an important role in the interaction between the beamlet and the target. Thus, the sputtering yield depends on if the surface have been previously collided.

Borrajo et al. Ref.[30] futher studied the effect of projectile molecular mass in sputtering yields using the ionic liquids EAN and EMIMIm of 108 u and 391 u respectively. Impact velocities ranged between 7-17 Km/s and experimental results showed a strong effect of molecular mass in the sputtering yields which increase for more massive molecules.

MD simulations on Silicon sputtering

Molecular Dynamics simulations have been used in order to fully understand the experimental sputering results obtained and to help determine the mechanism of sputtering. Moreover, the effect of the molecular mass, droplet diameter and initial kinetic energy of the droplet can be tested.

Saiz and Gamero-Castaño Ref.[31] used a pseudo-atom model to simulate the electrospraying of EMIMIm nanodroplets. They found that the atom ejection is produced by collision cascades and thermal sputtering. Collision cascades appear during the first moments of the impact when the thermal equilibrium is not reached yet and the interactions between projectiles and the target atoms are strong. Simulation results showed that the sputtering yield increases monotonically with the initial kinetic energy of the particles in the droplet and sigthly decreases with the droplet diameter. Sputtering for the EMIMIm appears for the first time at molecular energies of 12.7 eV.

Further molecular simulations by Borrajo et al. Ref.[30] and Saiz and Gamero-Castaño Ref.[10] confirmed that the higher the molecular mass of the projectile the higher are the sputtering yields. When kinetic energy is distributed between fewer more massively particles, the collisions produce knock-on atoms with higher energies that initiate secondary and tertiary collisions resulting in higher sputtering ratios. Moreover, results obtained showed that the energy transfered to the target and the energy dissipated also increase with the molecular mass of the projectile.

Experiments on Silicon amorphization

Amorphous thin layers on Silicon targets have been obtained by pulsed laser irradiation.[32] However, the amorphization mechanism here is not the melting and cool down of the crater region since the surface temperature achieved with laser irradiation is below the melting point. Thus, the responsible of the Si amorphization is a transition from a crystalline structure to a metallic beta-tin phase due to the high pressures achieved.[33]

Gamero et al. Ref.[2] studied the impact of beam electrosprayed nanodroplets not only into Si waffers but also on other single-crystals to prove that they could also be amorphized. In particular, they experimented with waffers of Si, Ge, GaAs, GaP, InAs and SiC using EMIMIm nanodroplets of 27 nm of diameter at velocities between 2.84 and 7.06 Km/s. Amorphization of thin layer surfaces was obtained for all the single-crystals but the SiC which could not be amorphized at the higher velocity of impact 7.06 Km/s. They predicted that the method of amorphization was the melting of the region surrounding the impact and posterior quenching at ultrafast cooling rates.

MD simulations on Silicon amorphization

Saiz and Gamero[18] performed MD simulations of the collision of a 10 nm nanodroplet into a Silicon target at 6.4 Km/s. Simulations showed that amorphization results from the melting and ultrafast quenching of the region around the impact area at cooling rates of $10^{13} K/s$. They conclude that the reason of amorphization with nanodroplet impacts is the significantly higher temperature fields and cooling rates compared to the ones obtained with macroprojectiles. Moreover, the amorphous region is obtained regardless of whether the fast kinetics prevent the Stilling-Weber potential from reproducing the physical amorphous phase.

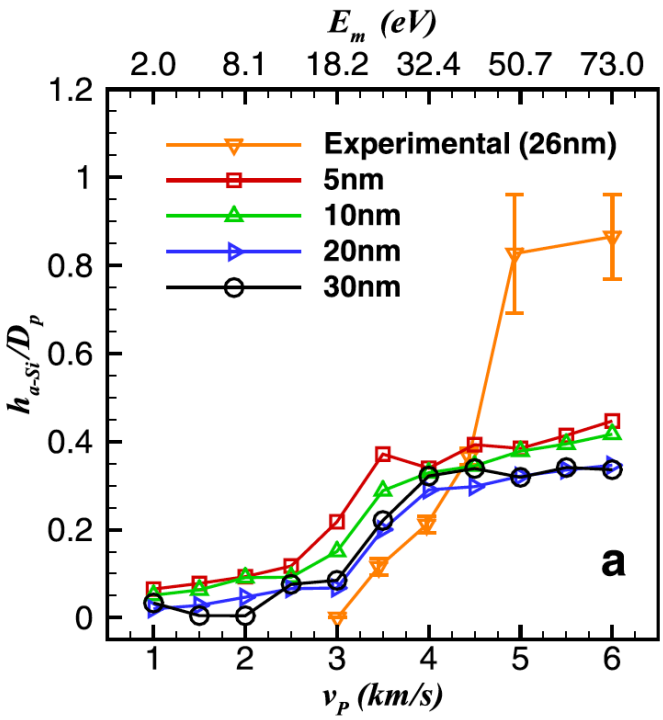

Figure 1.7: Amorphous thickness ratio to the droplet diameter vs kinetic energy for different projectile diameters.

Furthremore Saiz et al.[9] performed MD simulations on different diameter nanodroplets and at different velocities of impact in order to study its influence to the Silicon amorphization. The study shows that amorphization of the target appears at velocities near 3 Km/s and above. The thickness ratio to the projectile diameter increases with velocity until it reaches a plateu around 4 Km/s at an amorphous thickness of 0.4 times the droplet diameter as it is observed in Fig. 1.7. Additionally, they observed that the volume of the amorphous region scaled linearly both with increasing kinetic energy and projectile diameter as Fig. 1.8 depicts.

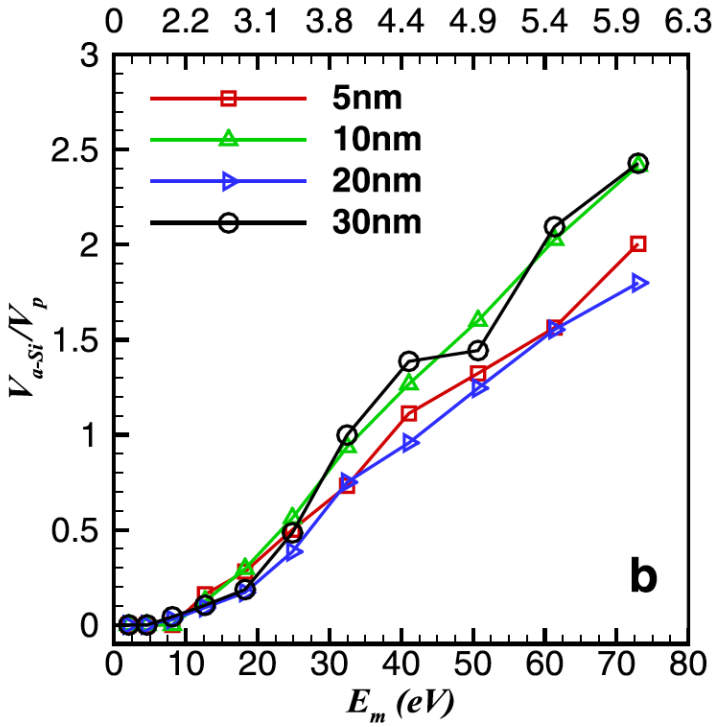

Figure 1.8: Volume of the amorphous Silicon region vs kinetic energy for different projectile diameters.

1.4 Objectives

The research detailed in this thesis is focused on introducing a new nanodroplet simulation model: the atomic/molecule model; and verifying that the outcome of the simulations is closer to experimental results than the one obtained when using the PA model. The objectives of the study include:

- Comparison of the crater temperature fields during the impact.
- Comparison of the sputtering of Silicon atoms.
- Comparison of the amorphized region after the collision.
- Investigation on the effect of having unbreakable bonds in the AM model.

1.5 Thesis Overview

- **Chapter 1:** Introduction of topic of interest.
- **Chapter 2:** Outline of the two models and properties of the simulations.
- **Chapter 3:** Discussion of the simulation results and comparison of the two models.
- **Chapter 4:** Summary of the findings in this study.

Chapter 2

Simulation Methods

2.1 Simulation setup

Simulations of the nanodroplet collisions are performed using the LAMMPS (Large-scale Atomic/Molecular Massively Parallel Simulator) software[34,35,18] and run in a HPC (High Performance Computing) cluster. A 3D grid global simulation box is used with a total of 36 processors: 4 in the z coordinate which is the direction of the collision and 3 processors for the x and y coordinates. The simulation box dimensions are 271.55 nm x 271.55 nm x 461.64 nm. It has periodic boundaries in the x and y directions in order to reproduce an infinite plane. Real units are used and simulations of the impact are run for 100 ps. Equations of motion are integrated with a timestep of 1fs for the first 10 ps[31] and 4 fs for the rest of the simulation.

2.2 Silicon target

The Silicon target is a rectangular (100) slab made of 755,000 Si atoms. The plane perpendicular to the collision measures 271.55 nm x 271.55 nm and slab has a depth of 203.66 nm in the direction of the impact. A Berendsen thermostat[36,37] is applied to all boundaries except the top face of the target in order to prevent shock wave reflections. The thickness of the thermostat is 2.17 nm for the lateral faces and 3.8 nm for the bottom one.[31] The slab temperature is set to 293 K and it is relaxed for 200 ps. This equilibrium configuration is used for the droplet impact simulations. A cubic diamond lattice is used for the Si target. The unit cell dimension is 5.431 Å and it contains 8 full Si atoms. Stillinger Weber potential energy function[15] is used in order to describe interactions in solid and liquid phases between Si atoms.

2.3 Nanodroplet models

The nanodroplets have a diameter of 5nm. Two different liquids are used in the simulations: Formamide and 1-Ethyl-3-methylimidazolium bis(trifluoromethylsulfonyl)imide (commonly referred to as EMIMIm). Both have been previously studied in experimental analysis.[38] The number of molecules per droplet is chosen in order to match the liquid density. Table 2.1 resumes the liquids parameters.

Table 2.1: Formamide and EMIMIm liquid molecule parameters.

	Density $[g/cm^3]$	**Molecular mass [u]**	**Atoms per molecule**	**Molecules per droplet**
Formamide	1.13	45.000	6	989
EMIMIm	1.53	391.312	34	153

Two molecule models are used in the droplet collision simulations. The first one is the pseudo atom model (PA)[18] previously used in MD simulations of nanodroplets collisions. In this model, each liquid molecule is represented as a particle (pseudo-atom) with the same molecular mass. The interactions between droplet molecules are only represented by the potential function between those particles. The new atomic-molecule model (AM) presented takes into account all atoms of each molecule. Intermolecular and intramolecular interactions are included and bonds can break. For the AM model, the initial atom coordinates are obtained by means of the Winmostar[39] software for the formamide molecule and from Ref.[40] for the EMIMIm. Each molecule is then brought to equilibrium at 0 K. The droplet is then built up using the PACKMOL software[41] which arranges all molecules evenly spaced inside a 5 nm diameter sphere so that initially they do not interact.

2.4 Interactive potentials

Interactive forces between particles in the PA model and between atoms that belong to different molecules in the AM model are obtained using the Ziegler-Biersack-Littmark (ZBL) potential function equations.[16,30] The ZBL potential describes accurately the high energy collisions between particles and only depends on the atomic number. Bonds in the AM model are defined with a combination of the ZBL and Morse[17] potential functions. The Morse

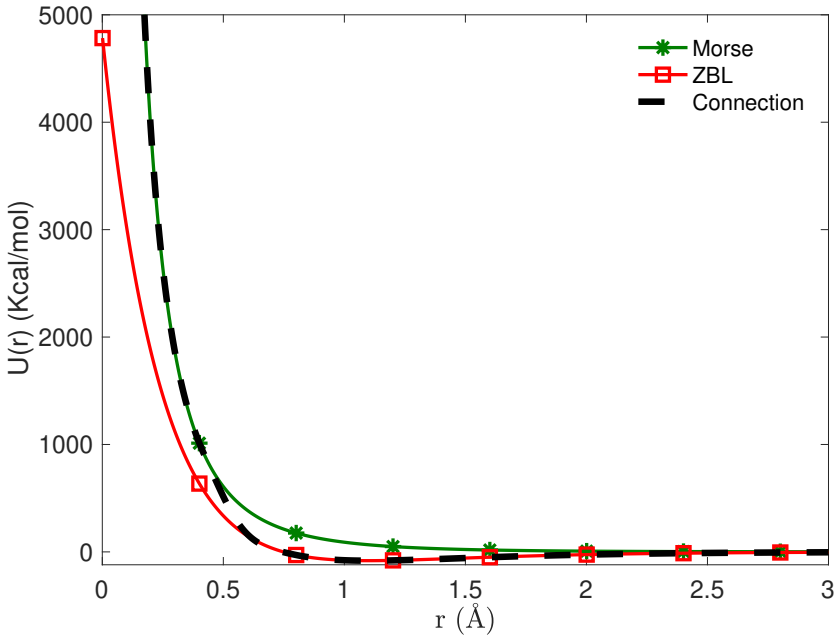

Figure 2.1: Connection of the ZBL and Morse potentials by means of an interpolation spline for the C-H bond in the Formamide molecule.

potential is a convenient interatomic interaction potential because it explicitly includes the effects of bond breaking by including a potential minimum of dissociation energy. However, a ZBL potential is still necessary to reproduce collisions. Therefore, the ZBL potential is smoothly connected to the Morse potential at a bond length short enough where collisions may occur. The connection is achieved by a 5 order polynomial exponential interpolation as seen in Fig. 2.1. The 6 polynomial coefficients are obtained by matching the potential function value, the first and the second derivatives at the inner and outer cutoffs. Those cutoffs are determined minimizing the gap of the interpolation spline that will connect both potentials.

The Morse potential function is shown in Eq. 1.16. Tables 2.2 and 2.3 collect the Morse potential parameters for both liquids. The spring constant K_e and the equilibrium bond length r_0 are obtained from Ref.[42] for the case of formamide and from Ref[43] for the EMIMIm. Dissociation energies are extracted from the Y. R. Luo *Comprehensive handbook*

Table 2.2: Formamide Morse potential parameters.

ID	**bond**	r_0 [Å]	$\mathbf{k_r}$ [**Kcal/mol/Å^2**]	$\mathbf{D_e}$ [**Kcal/mol**]	**a** [**1**/Å]
1	C-H	1.100	635.4	81.7	1.972
2	C-N	1.360	860.0	100.8	2.065
3	C-O	1.230	1300.0	109.4	2.438
4	N-H	1.000	960.0	108.5	2.103

Table 2.3: EMIMIm Morse potential parameters.

ID	**Bond**	$\mathbf{r_0}$ [Å]	$\mathbf{k_r}$ [**Kcal/mol/Å^2**]	$\mathbf{D_e}$ [**Kcal/mol**]	**a** [**1**/Å]
1	C-N	1.337	800.0	55.0	2.697
2	C-N	1.382	800.0	55.0	2.697
3	C-N	1.476	440.0	65.0	1.840
4	C-N	1.476	440.0	65.0	1.840
5	C-H	1.078	680.0	119.0	1.690
6	C-H	1.078	730.0	119.0	1.751
7	C-C	1.361	820.0	100.0	2.025
8	C-H	1.090	618.0	90.0	1.853
9	C-H	1.090	618.0	90.0	1.853
10	C-H	1.531	445.0	100.0	1.492
11	C-H	1.094	644.0	90.0	1.892
12	S-N	1.570	744.0	92.0	2.011
13	S-O	1.442	1274.1	122.0	2.285
14	C-S	1.818	470.8	90.0	1.617
15	C-F	1.323	883.6	125.0	1.880

of chemical bond energies.[44] For the EMIMIm case, dissociation bond energies are obtained from same chemical groups in other molecules. Due to this approximation, a complementary model is simulated with larger dissociation energies so that bonds do not break. A bond breaks at a length where its potential energy is 1% of the dissociation energy.

2.5 Nanodroplet parameters

Both droplet models are simulated for 5 different initial kinetic energies. Velocities are chosen to match those energies according to the equipartion theorem. A characteristic time t_c

is defined as $t_c = D_p/v_p$. In order to obtain a better comparison between models, a dimensionless time $t^* = t/t_c$ is used. Table 2.4 resumes the five cases simulated.

Local temperature is computed at each j-th Si atom position using the method of average kinetic energy of neighboring atoms (Eq. 2.1) within a spherical control volume of radius 10.8[18] Å:

$$T(\mathbf{x}_j) = \frac{\sum_{i=1}^{N} m_i(v_i - \langle v_j \rangle)^2}{3K_B N} \tag{2.1}$$

N is the total number of neighbor atoms, k_B is the Boltzman constant, m_i and v_i are the mass and velocity of the i-th neighbor. $\langle v_j \rangle$ is the average velocity of all particles within the spherical control volume centered on the j-th Si atom. Collision visualizations are obtained using the Ovito software[45] as seen in Fig. 3.1.

Table 2.4: Droplet kinetic energy and corresponding velocities and characteristic times for the two molecule types.

Droplet energy (KeV)		**2.81**	**5.00**	**7.81**	**11.25**	**15.31**
Formamide	**Velocity [km/s]**	3.491	4.654	5.818	6.982	8.145
	tc [ps]	1.432	1.074	0,859	0.716	0.614
EMIMIm	**Velocity [km/s]**	3.000	4.000	5.000	6.000	7.000
	tc [ps]	1.667	1.250	1.000	0.833	0.714

Chapter 3

Results

3.1 Temperature field

Fig. 3.1 shows a target slice aligned with the collision plane at $t/t_c = 1$. The target temperature computed at each Si particle location is depicted by a color scale. White spheres represent pseudo-atoms in the PA models (Fig. 3.1a and Fig. 3.1c) while the AM models (Fig. 3.1b and Fig. 3.1d) shows all the molecule atoms. The velocity of the impact is 5.0 km/s for the EMIMIm and 5.818 km/s for the formamide droplet. After the impact, a large amount of energy is transferred to the slab increasing its surface temperature. PA models for both liquid types show higher temperatures around the collided droplet than the AM models. Temperatures exceed 2000 K in the PA models, which is above the Silicon melting point (1685 K at 1 atm). Tempereature fields for the PA models are different for the EMIMIm and formamide whereas the AM models are quite similar for both liquids.

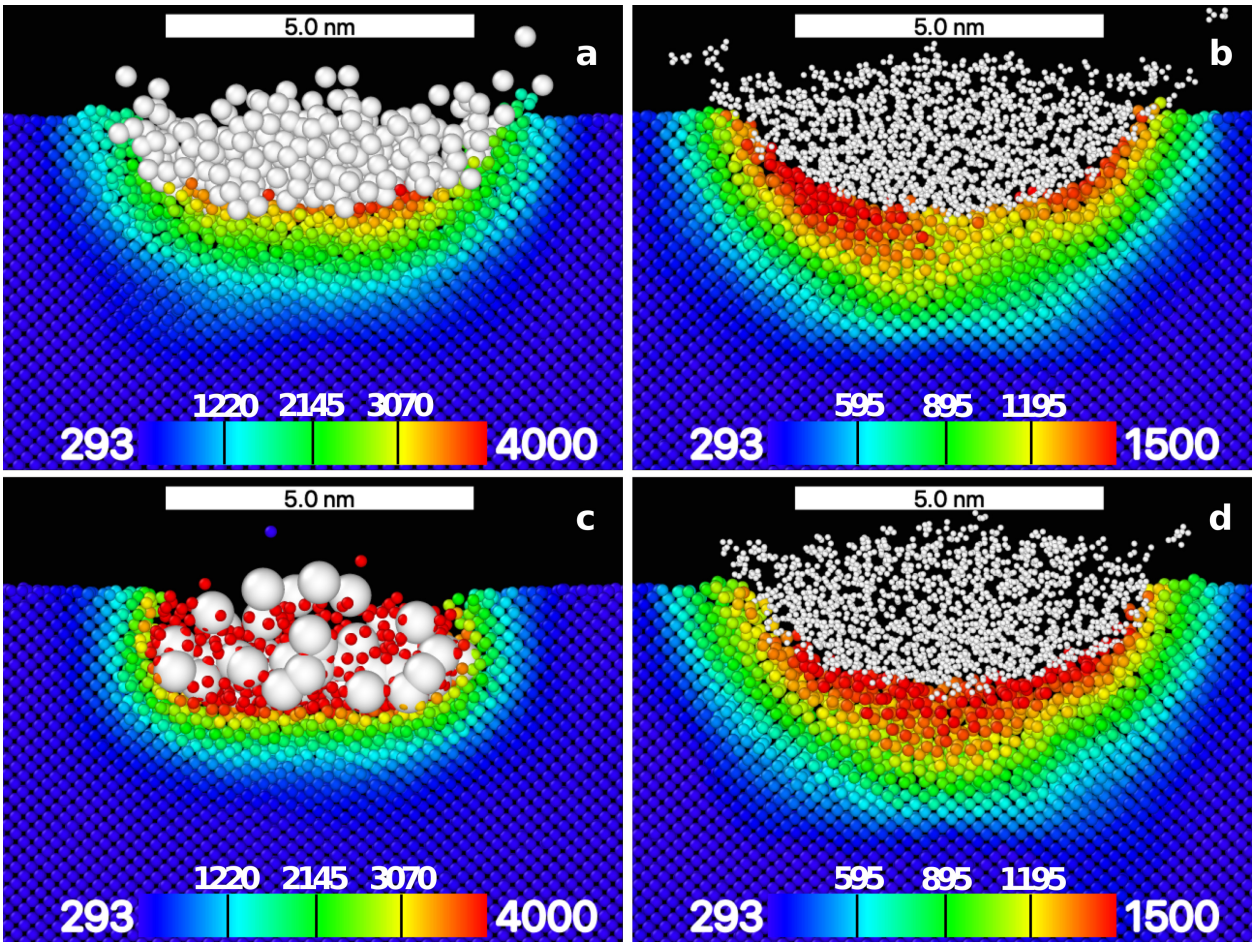

Figure 3.1: Cross sectional temperature map view of the four models collisions at $t/t_c = 1$, with velocities of 5 km/s for the EMIMIm and 5.818 km/s for the formamide. (a) Formamide PA model; (b) Formamide AM model; (c) EMIMIm PA model; (d) EMIMIm AM model.

3.2 Energy transfer

During the droplet impact, most of the initial kinetic energy of the projectile $E_{K,p}$ is transferred to the target surface in the form of thermal energy $E_{Th,t}$, translational energy $E_{CM,t}$ and potential energy $E_{P,t}$. The energy retained by the droplet after the collision is due to the droplet rebound. Fig. 3.2 plots the evolution in time of these energies for the four different models for velocities of 7 km/s in the case of the EMIMIm and 8.145 km/s for the formamide. In order to compare energy values to the initial droplet kinetic energy, target energies are normalized to their initial value and scaled with the initial kinetic energy of the droplet (15.31 keV). Thermal energy is computed by adding the respective value of each k-th particle $E_{Th}^k = 1.5 K_B T^k$ where T^k is obtained as defined in Eq. 2.1. Translational energy is computed using the average velocity of the 10.8 Å spherical volumes used to obtain particle temperatures. As obtained in Ref[10], most of the droplet kinetic energy is lost and transferred to the slab in form of potential energy due to the large atom disorder around the collision. The rest is exchanged in form of thermal and translational energy. The latter has a peak at the moment of the impact and vanishes soon after that. The kinetic energy after the impact for the EMIMIm PA droplet model in Fig. 3.2a is almost null. The colision is inelastic, the droplet regains no kinetic energy after the colision and remains close to the surface. On the other hand, the AM droplet models regain some kinetic energy after the collision and rebound from the surface. Thermal energy acquired by the target in the EMIMIm PA model is almost twice the value obtained by the AM models. There is no appreciable distinction between the translation energy in the formamide PA and AM models whereas, it is lower for the EMIMIm PA case. This is as a result of the highly energetic pseudo-atoms penetration into the slab. EMIMIm droplets are build up only by 153 pseudo atoms. Each of them carries 100.08 eV for the higher velocity case of 15.31 keV droplet projectile. There are 989 pseudo atoms in the formamide droplet and they only carry 15.48 eV for the same conditions. The atomic-molecule model presents even less particle kinetic energy values.

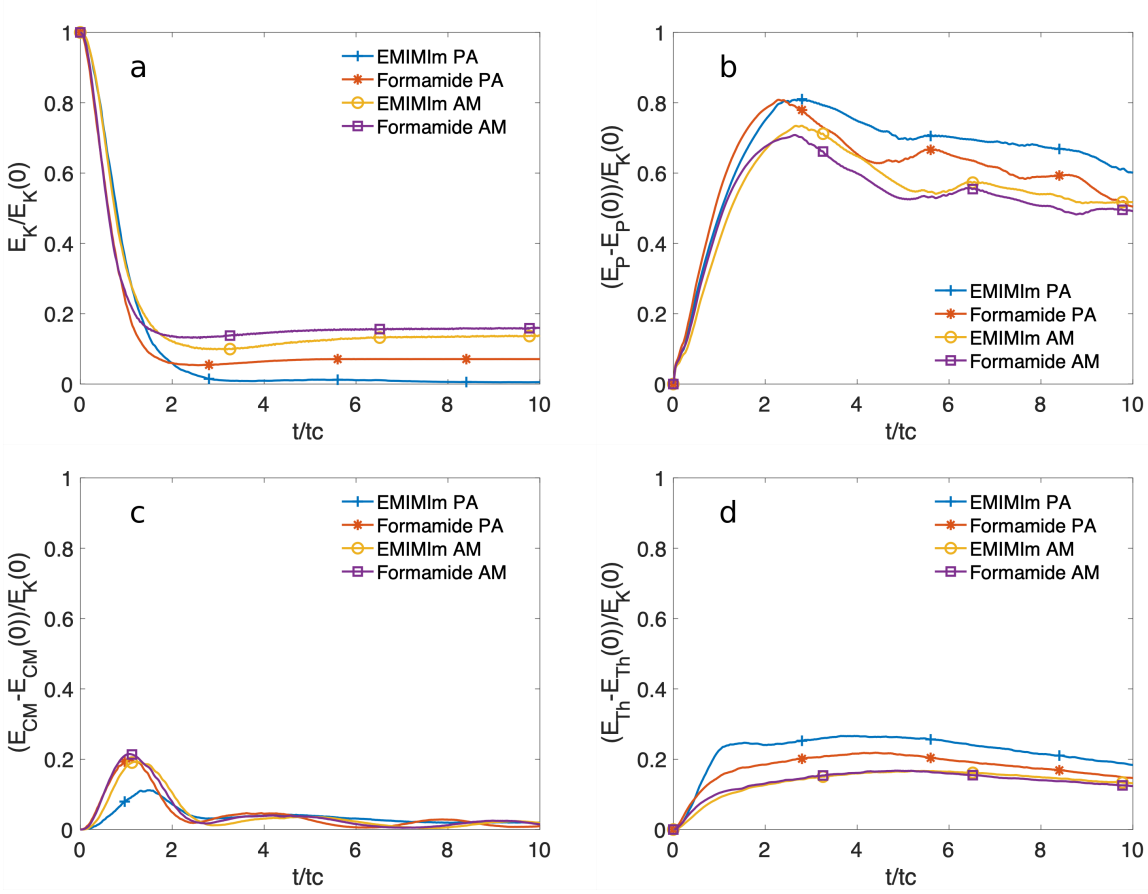

Figure 3.2: Evolution in time of the (a) droplet kinetic energy and (b) potential, (c) thermal, (d) translational target energies for the EMIMIm and formamide PA and AM models for a droplet initial kinetic energy of 15.31 KeV.

The formamide AM droplet has a total of 5934 particles with an average kinetic energy per atom of 2.58 eV ranging between 0.34 eV and 5.5 eV. The EMIMIm AM droplet is build up by 5236 particles with 2.92 eV average kinetic energy per atom ranging between 0.25 eV and 8.13 eV. The collision of fewer but more energetic projectiles in the EMIMIm PA case produce knock-on atoms with higher energies that generate more energetic secondary and tertiary knock-on atoms.[10] This is also appreciated in Fig. 3.3c, these knock-on atoms contained in the outer crater layer are at extremely high temperatures. Moreover, the atoms in the AM model are connected by intramolecular potentials so that they push each other filling the gaps between droplet molecules resulting in a macroscopic rebound of the droplet. On the other hand, the PA droplet molecules are only connected by the repelling ZBL in-

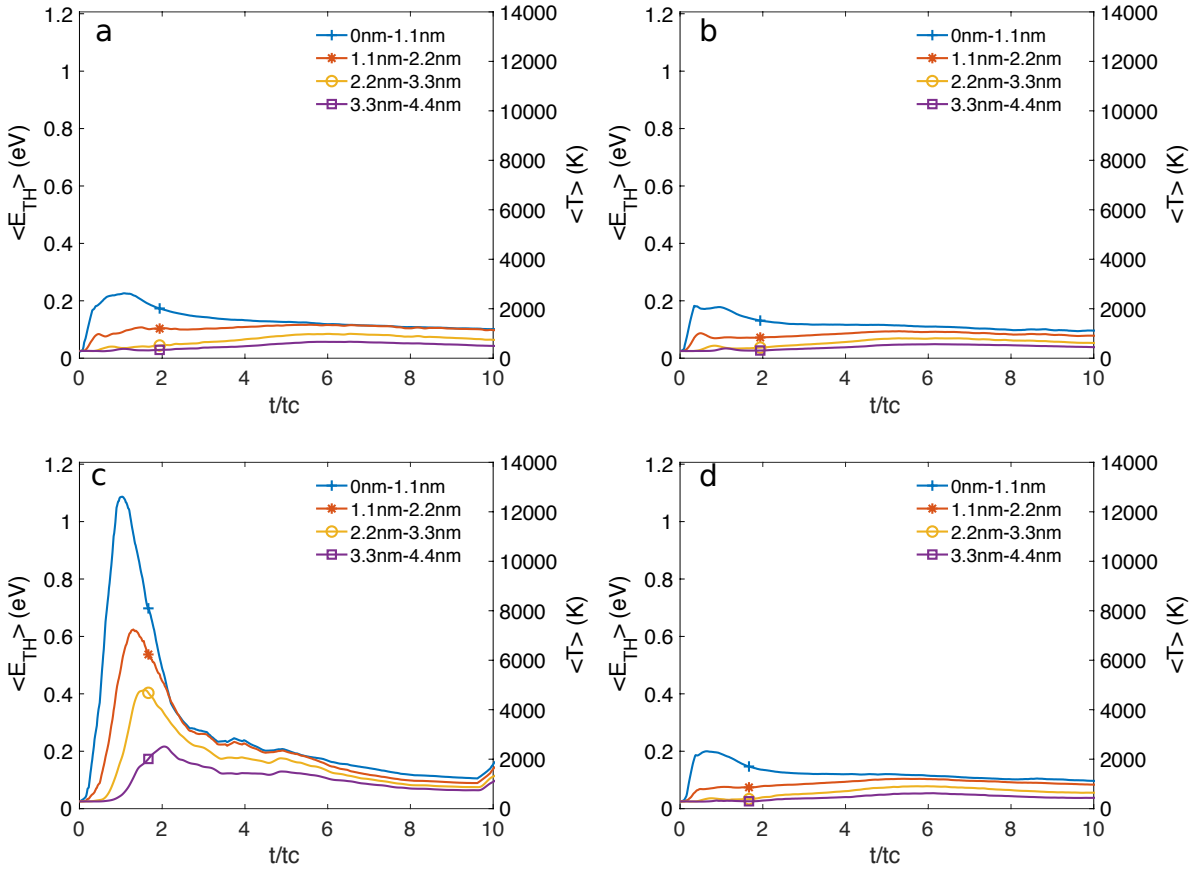

Figure 3.3: Average layer temperature for the four models simulated at the highest droplet initial kinetic energy. (a) Formamide PA model at 8.145 km/s; (b) Formamide AM model at 8.145 km/s; (c) EMIMIm PA model at 7 km/s; (d) EMIMIm AM model at 7 km/s.

termolecular potential. They repel Si atoms isotropically resulting in a further penetration into the slab and, therefore, the droplet does not bounce back as observed in Fig. 3.2(a).

Fig. 3.3 shows the average crater layer thermal energy for the four models simulated at the highest droplet kinetic energy. Each layer has a width of 1.1 nm perpendicular to the crater surface. The EMIMIm PA droplet transmits several times more thermal energy to the outer surface layers than the other cases. The outermost layer has an average temperature greater than 12000 K at the moment of the impact whereas the AM and the formamide PA models only reach around 2000 K.

3.3 Collision crater

Fig. 3.4 shows the crater at two different states of the collision ($t/t_c = 4$ and $t/t_c = 8$) for the EMIMIm liquid PA models (pictures a-d) and AM models (pictures e-h) at velocities 5 km/s and 7 km/s. In Fig. 3.4e-h the AM model droplet rebounds with no atoms remaining inside the slab leaving deeper craters for higher velocities. Fig. 3.4c (corresponding to the EMIMIm PA model at 7 km/s at $t/t_c = 4$) shows how the projectile particles penetrate the slab much further than the ones in Fig. 3.4a which corresponds to the same model but velocity 5 km/s. In Fig. 3.4b and Fig. 3.4d, which correspond to $t/t_c = 8$, the pseudo-atoms of the 5 km/s case rebound from the surface leaving only a 35% of the particles inside the slab while at 7 km/s 95% of them remain inside the target after the collision. This causes that, at some point, craters originated from collisions at higher velocities are more superficial than the ones corresponding to lower velocities. Melted Silicon rapidly fills the gap generated by the 7 km/s droplet and cools down. When the impacts are at lower velocities the Si surface cools down while the droplet particles are bouncing back which leaves a deeper crater. This phenomen can be appreciated in Fig. 3.5.

Fig. 3.5 depicts the crater left after 100 ps of simulation by the four models for all the different droplet initial kinetic energies. Both AM models and the PA model for the formamide show deeper holes for increasing impact velocities and AM and PA formamide projectiles leave comparable craters of size and depth. The EMIMIm PA model shows the same behavior up to 5 km/s, at that point the crater starts to become more superficial due to the pseudo-atoms penetration into the slab.

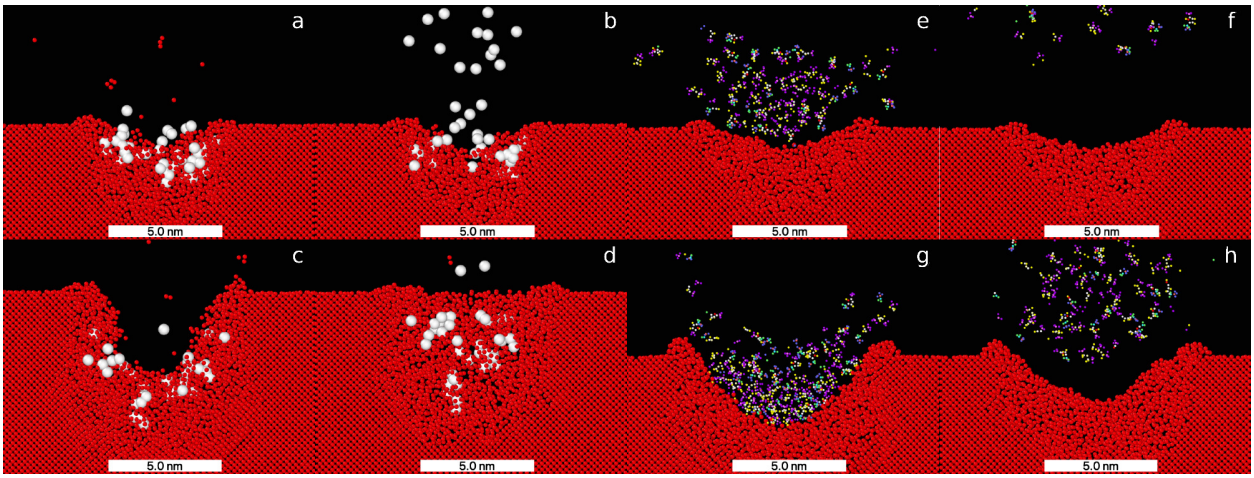

Figure 3.4: 4 EMIMIm collision of the projectile for the PA model and AM model at velocities 5 km/s and 7 km/s and for $t/t_c = 4$ and $t/t_c = 8$. (a) PA at 5 km/s for $t/t_c = 4$; (b) PA at 5 km/s for $t/t_c = 8$; (c) PA at 7 km/s for $t/t_c = 4$; (d) PA at 7 km/s for $t/t_c = 8$; (e) AM at 5 km/s for $t/t_c = 4$; (f) AM at 5 km/s for $t/t_c = 8$; (g) AM at 7 km/s for $t/t_c = 4$; (h) AM at 7 km/s for $t/t_c = 8$.

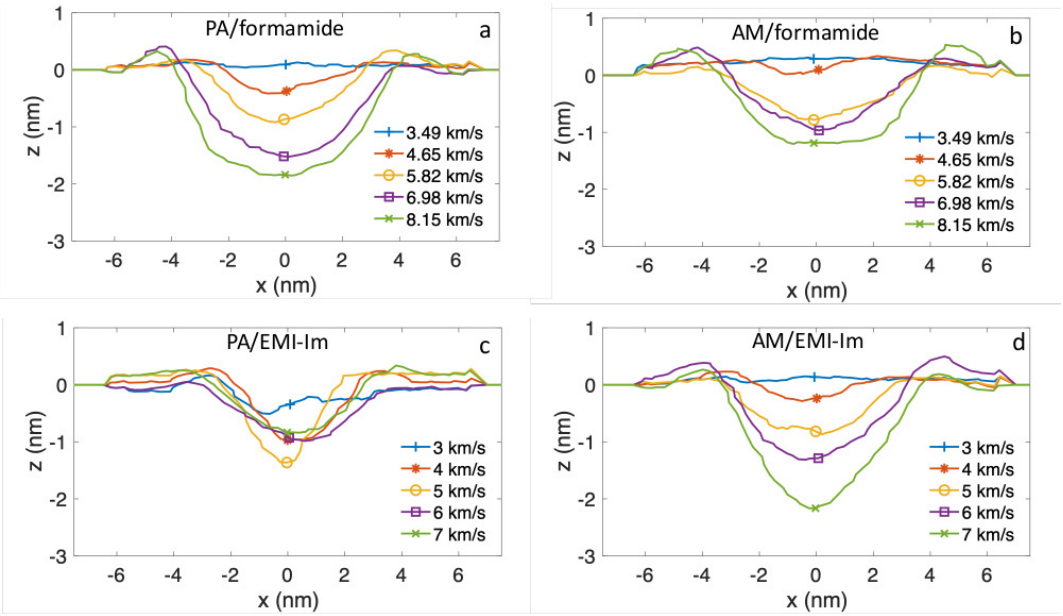

Figure 3.5: Craters left after 100 ps of simulation for the AM and PA models for the five different droplet initial kinetic energies.

3.4 Sputtering

The number of sputtered atoms is represented in Table 3.1. Sputtering for PA models is low for the formmide droplet but considerable for the EMIMIm. There are no Si atoms sputtered when using AM models. However, experimental results obtained in Ref[31] showed sputtering for the same droplet diameter and velocities studied in this article. The reason to that is that experimental sputtering is obtained after a sequencial bombardment of droplets. The first droplets collisions amorphize and reshape the slab surface leaving a target more susceptible to sputtering with the follow up impacts. On the other hand, the simulations only take into account a single droplet collision into a perfectly shaped Si surface. Thus, results obtained by the AM model are considered valid since sputtering is not possible for the first droplet impact. Sputtering obtained by the EMIMIm PA model is due to the high molecular mass of the liquid. EMIMIm pseudo-atoms have a substantially greater energy per particle than the other models. The resulting knock-on atoms of the collision are more energetic (as seen in Fig. 3.3c) so that they can overcome the surface binding and end up being ejected. But this is not the real mechanism of sputtering observed in electrospraying experiments. The AM models and also the formamide PA model have a significantly larger number of particles than the EMIMIm PA droplet. The energy per particle is low and sputtering can not be achieved during the first droplet impacts.

Table 3.1: Number of sputtered Si atoms for the PA and AM EMIMIm and formamide models at the five initial droplet kinetic.

Drolet energy (KeV)		**2.81**	**5.00**	**7.81**	**11.25**	**15.31**
AM	**EMIMIm**	0	0	0	0	0
	Formamide	0	0	0	0	0
PA	**EMIMIm**	7	57	79	77	115
	Formamide	0	0	0	1	2

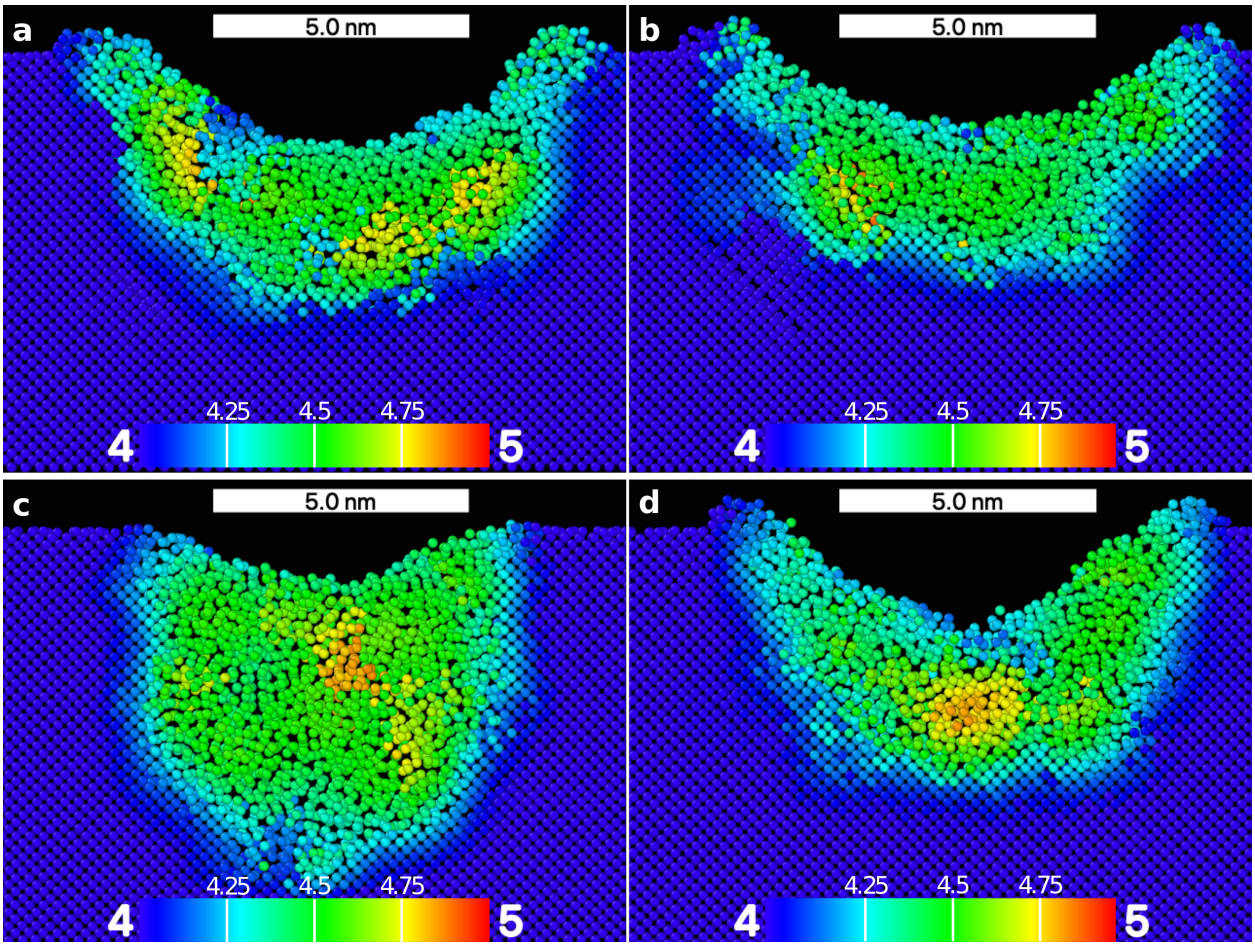

Figure 3.6: Coordination number field after 100 ps of simulation for the four models at the highest droplet kinetic energy. (a) Formamide PA model at 8.145 km/s; (b) Formamide AM model at 8.145 km/s; (c) EMIMIm PA model at 7 km/s; (d) EMIMIm AM model at 7 km/s.

3.5 Amorphization. Coordination number

Fig. 3.6 shows the coordination number field after 100 ps of simulation for the highest droplet initial kinetic energy collision. The blue region represents the Si atoms in crystalline phase with coordination number CN = 4. Green particles have a coordination number around CN = 4.3 and yellow regions correspond to CN = 4.6. The latter two cases are respectively Si atoms in amorphous and glassy phase.[18] Both result from fast quenching at different cooling ratios. Formamide AM and PA models show similar structural phases. The PA model presents some more glassy phase regions because it has been cooled down from higher temperatures. The EMIMIm PA droplet presents a deeper amorphous region than the AM model as a result of the particle penetration into the slab at this velocity range.

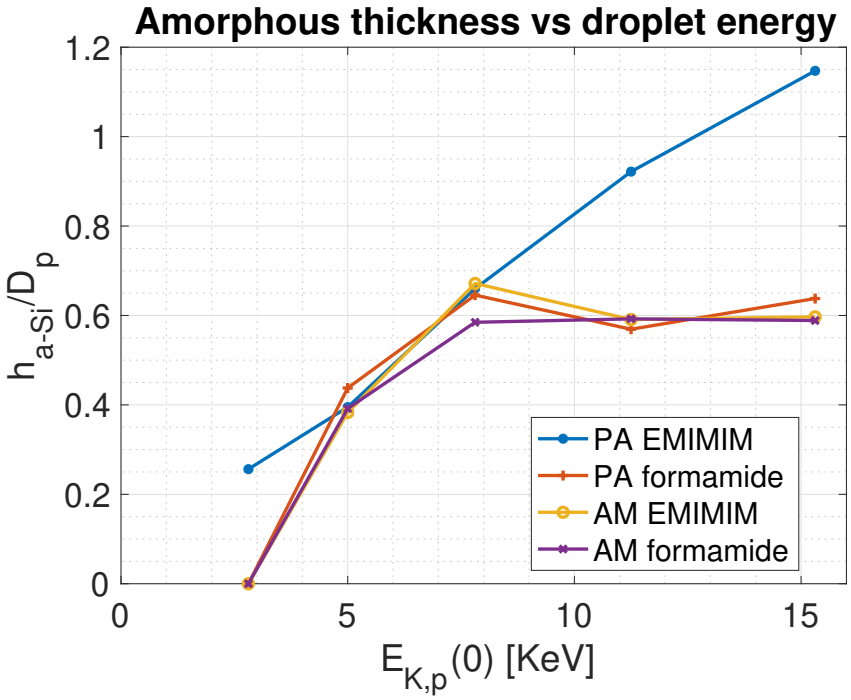

Figure 3.7: Amorphous Silicon phase depth in function of initial droplet kinetic energy for the four different models.

Fig. 3.7 depicts information about the amorphous depth of the four different models for different initial droplet energies. The amorphous region depth is taken from the bottom of the collision crater and it is scaled with the droplet diameter for comparison purposes. As pointed out in Ref[9], amorphous region does not appear until droplet energies higher than 3 KeV. From that point, the amorphous layer depth increases until reaching an asymptote at a ratio of 0.6 times the droplet diameter. The EMIMIm PA model leaves a deeper amorphous phase region due to the further penetration of pseudo-atoms into the slab which melts a larger volume of Silicon that later cools down and changes to an amorphous phase.

3.6 AM model broken bonds

Fig. 3.8 shows the ratio of broken bonds for the formamide and EMIMIm projectiles at different droplet initial kinetic energies for the atomic-molecule model. A bond is considered to dissociate at a distance where its energy is 1% of the dissociation energy D_e. Only a low fraction of formamide bonds break. However, the EMIMIm model presents high fractions of broken bonds, specially for the more energized droplets which reach almost 40% of broken bonds for some types. Fig. 3.8b shows that the lower the dissociation energy the higher the probability of that bond to be broken after the collision. Nitrogen-Carbon bonds located in the EMIMIm cation ring are the ones that tend to break more since they have the lower dissociation energy. One can observe that there are different values of broken bonds for same dissociation energies. They correspond to same bond types located at different positions of the molecule. This implies that the break of a bond not only depends on the dissociation energy but also on its location. At $D_e = 2.4$ eV, 35% of C-N bonds break from the N-CH2-N side of the cation ring whereas a 38% of C-N break on the other side of the ring. At $D_e = 2.8$ eV, results show that 25% of C-N bonds break releasing an ethyl radical located in

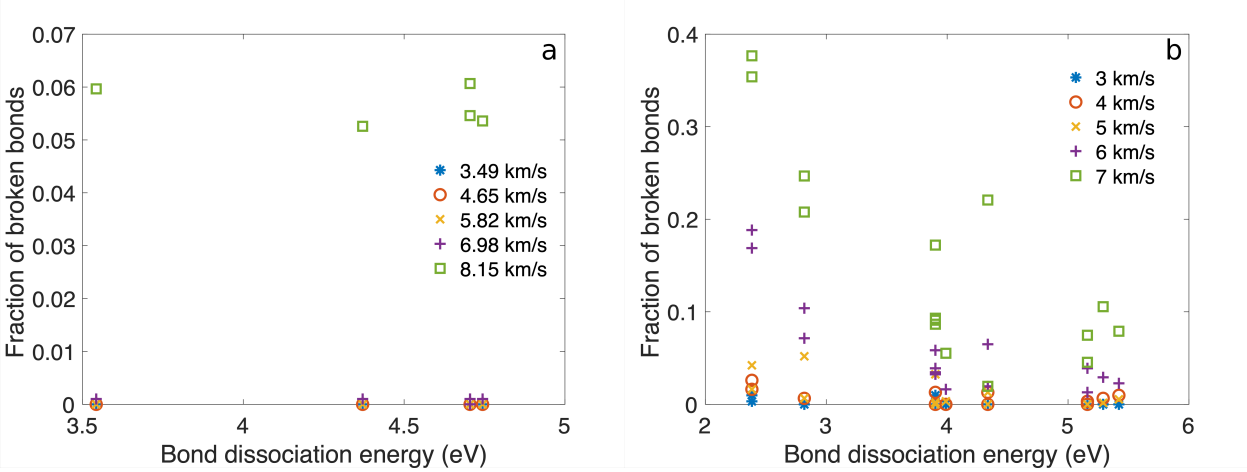

Figure 3.8: Broken bonds ratio for the formamide (a) and EMIMIm (b) AM droplet models for different projectile initial kinetic energies

the cation while 21% break freeing a methyl. Furthermore, there are four bonds with same dissociation energy at around $D_e = 3.9$ eV. The bond with a higher fraction corresponds to the C-S bond located in the EMIMIm anion whereas the other three types correspond to the C-H bonds from the methyl and ethyl in the cation.

3.7 Strong-bond AM model

Due to the lack of experimental research on the EMIMIm bonds, bond dissociation energies have been obtained from values of same chemical groups located in other molecules. For this reason, additional simulations have been performed with bond dissociation energies ten times stronger than the ones previously treated. These bonds do not break during the simulation. The fraction of initial kinetic energy employed to dissociate the bonds is negligible. The analysis verifies that the AM model with unbreakable bonds does not significantly affect the outcome of the simulations.

Fig. 3.9 depicts the droplet kinetic energy, thermal, translational and potential target energies of the EMIMIm AM models with normal and unbreakable bonds. It is observed

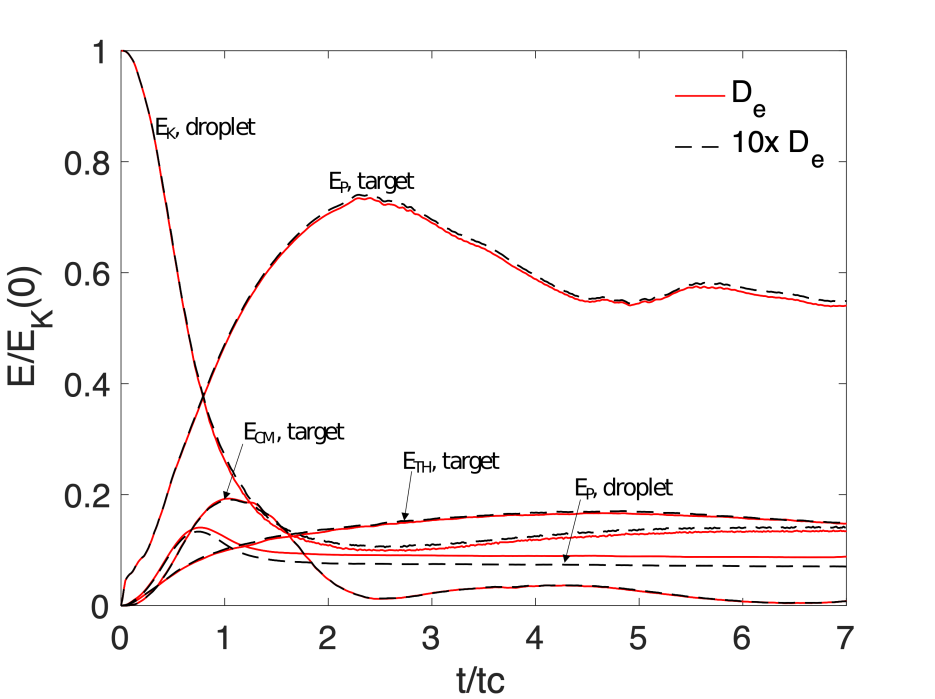

Figure 3.9: Comparison of the kinetic droplet energy and thermal, translational and potential target energies between the EMIMIm AM model and the EMIMIm AM model with strong bonds for a velocity of 7 km/s.

that thermal and translational target energies are identical whereas the droplet kinetic energy and target potential energy are slightly greater for the strong-bond model. The reason is that the small energy that has not been employed to break molecule bonds is used to increase the potential target of the slab and to increase the rebound of the droplet. Fig. 3.10 shows the coordination number field after 100 ps using stron bonds. It presents the same structural phases than the previous AM model.

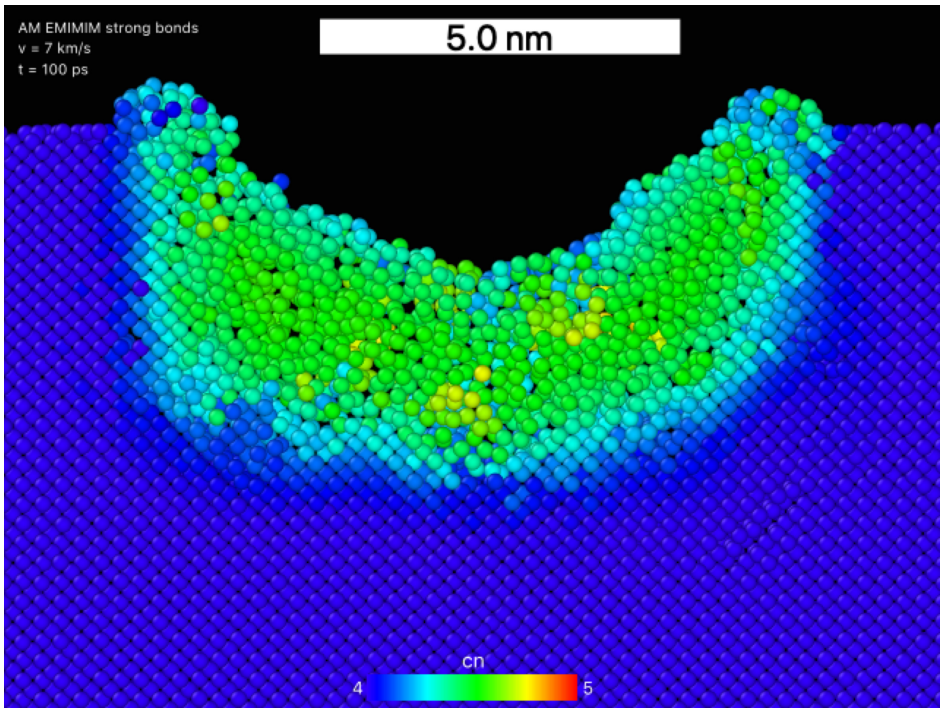

Figure 3.10: Coordination number field after 100 ps for the EMIMIm AM model with unbreakable bonds for a velocity of 7 km/s.

Chapter 4

Conclusion

4.1 Summary

The PA model show much higher temperature fields than the AM for both liquids. The thermal energy absorbed by the slab after the pseudo-atom droplet collision is significantly larger than the absorbed after the atomic/molecule projectile one. Droplets with high initial kinetic energy rebound when using the AM model but they do not for the PA simulations.

Pseudo-atoms particles for energetic projectiles carry large amount of energy per particle, specially the EMIMIm liquid. These particles penetrate further into the Silicon slab and melt a greater volume of Silicon. The crater left in this case is shallower than for lower velocities. In contrast, the AM model leaves deeper craters for higher droplet kinetic energies because there is no particle penetration.

No Si atoms are sputtered when using AM models. This is expected for a collision of a single droplet into a perfectly shaped Si surface. However, the pseudo-atom droplets cause

sputtering due to the high energy per particle they carry. The massive particles of this model directly knock on atoms from the surface. The PA model does not reproduce the real mechanism of sputtering of electrosprayed nanodroplets observed in experimental studies.

Both models show a similar amorphization of the Silicon for the Formamide projectiles but not for the EMIMIm. PA droplet collisions develope a larger volume of amorphous Silicon than the ones simulated using the AM model. This is again related to the high atomic mass of the EMIMIm. Furthermore, the depth of the amorphous region asymptotes as expected at a value of 0.6 for both AM models and the formamide PA one. However, it does not for the EMIMIm liquid, which continues to increase reaching values of 1.

Bonds in the AM model start breaking for droplet kinetic energies greater than 10 KeV. The ratio of broken bonds is higher for the lower bond dissociation energies. Additionally, it is observed that the ratio of broken bonds also depends on their location inside the molecule.

Finally, the strong-bond analysis for the EMIMIm molecule shows that the droplet kinetic energy employed to break bonds is negligible and the results obtained are almost the same to the ones of breakable bonds. The strong-bond model shows a slightly bigger rebound of the droplet and a minor increase of the target potential energy.

An atomic/molecule model with unbreakable bonds is the better option for Molecular Dynamics simulations of nanodroplets collisions.

4.2 Recommendations for Future Work

The EMIMIm PA model shows substantial different results than the other three models simulated. Moreover, penetration of this particles into the Si target from a certain level of initial kinetic energy causes that the remaining crater to be deeper at lower impact velocities. As seen, one of the reasons is the high energetic particles from which the nanodroplet is built up in this configuration. Additional simulations on this model could determine the nature of this phenomena and if it is physically possible.

As expected, sputtering yields for a single collision of AM nanodroplets are null. In order to relate sputtering ratios to electrospraying experimental results, new simulations of the bombardment of nanodroplets into a Si target should be performed. Non zero sputtering yields should be obtained from these simulations of collisions into an existing amorphized crater.

A considerable number of bonds break in the AM models. It has been observed that the probability of a bond to break depends on its dissociation energy as well as its location inside the molecule. However, the chemistry after a bond breaks has not been taken into account since new bonds cannot be formed. Adding a new interacting potential to the model that generates new connections after a bond breaks would provide interesting data about the formation of new chemical groups after the collisions.

The Morse potential function parameters for the EMIMIm AM model were obtained from same chemical groups of other molecules. Although results show that the energy consumed breaking bonds is low compared to the droplet initial kinetic energy, obtaining experimentally those parameters would result in more accurate simulations.

Bibliography

[1] R. Borrajo-Pelaez, E. Grustan-Gutierrez, and M. Gamero-Castaño, "Sputtering of Si, SiC, InAs, InP, Ge, GaAs, GaSb, and GaN by electrosprayed nanodroplets," *Journal of Applied Physics*, vol. 114, no. 18, 2013.

[2] M. Gamero-Castaño, A. Torrents, R. Borrajo-Pelaez, and J. G. Zheng, "Amorphization of hard crystalline materials by electrosprayed nanodroplet impact," *Journal of Applied Physics*, vol. 116, no. 17, pp. 1–7, 2014.

[3] P. Sigmund, "Theory of Sputtering. I. Sputtering Yield of Amorphous and Polycrystalline Targets," *Physical Review*, vol. 184, no. 2, pp. 383–416, aug 1969.

[4] P. Sigmund, "Energy density and time constant of heavy-ion-induced elastic-collision spikes in solids," *Applied Physics Letters*, vol. 25, no. 3, pp. 169–171, aug 1974.

[5] J. Samela and K. Nordlund, "Origin of nonlinear sputtering during nanocluster bombardment of metals," *Physical Review B*, vol. 76, no. 12, p. 125434, sep 2007.

[6] K. K. Tanaka, *Amorphous silicon*. Wiley, 1999.

[7] R. A. Street, *Technology and applications of amorphous silicon*. Springer, 2000.

[8] R. Borrajo-Pelaez and M. Gamero-Castaño, "Ultrafast physical sputtering of GaN by electrosprayed nanodroplet beams," *Materials Letters*, vol. 159, pp. 110–113, 2015.

[9] F. Saiz, R. Borrajo-Pelaez, and M. Gamero-Castanof, "The influence of the projectile's velocity and diameter on the amorphization of silicon by electrosprayed nanodroplets," *Journal of Applied Physics*, vol. 114, no. 3, pp. 1–7, 2013.

[10] F. Saiz and M. Gamero-Castaño, "Molecular dynamics of nanodroplet impact: The effect of the projectile's molecular mass on sputtering," *AIP Advances*, vol. 6, no. 6, 2016.

[11] T. Morishita, "High Density Amorphous Form and Polyamorphic Transformations of Silicon," *Physical Review Letters*, vol. 93, no. 5, p. 055503, jul 2004.

[12] M. P. Allen, *Introduction to Molecular Dynamics Simulation*, 2004, vol. 23.

[13] F. Saiz Poyatos and Fernan, "Atomistic modeling of the hypervelocity impact of electrosprayed nanodroplets," Ph.D. dissertation, 2013.

[14] J. V. Goicochea, M. Madrid, and C. Amon, "Thermal Properties for Bulk Silicon Based on the Determination of Relaxation Times Using Molecular Dynamics," *Journal of Heat Transfer*, vol. 132, no. 1, p. 012401, jan 2010.

[15] F. H. Stillinger and T. A. Weber, "Computer simulation of local order in condensed phases of silicon," *Physical Review B*, 1985.

[16] J. F. Ziegler and J. P. Biersack, *The Stopping and Range of Ions in Matter*. Boston, MA: Springer US, 1985.

[17] P. M. Morse, "Diatomic Molecules According to the Wave Mechanics. II. Vibrational Levels," *Physical Review*, vol. 34, no. 1, pp. 57–64, jul 1929.

[18] F. Saiz and M. Gamero-Castaño, "Amorphization of silicon induced by nanodroplet impact: A molecular dynamics study," *Journal of Applied Physics*, vol. 112, no. 5, pp. 1–6, 2012.

[19] R. Behrisch, Ed., *Sputtering by Particle Bombardment I*, ser. Topics in Applied Physics. Berlin, Heidelberg: Springer Berlin Heidelberg, 1981, vol. 47.

[20] P. Sigmund and Peter, "Mechanisms and theory of physical sputtering by particle impact," *Nuclear Instruments and Methods in Physics Research Section B: Beam Interactions with Materials and Atoms*, vol. 27, no. 1, pp. 1–20, jun 1987.

[21] T. Schenkel, M. A. Briere, H. Schmidt-Böcking, K. Bethge, and D. H. Schneider, "Electronic Sputtering of Thin Conductors by Neutralization of Slow Highly Charged Ions," *Physical Review Letters*, vol. 78, no. 12, pp. 2481–2484, mar 1997.

[22] S. D. Gilev and A. M. Trubachev, "Metallization of silicon in a shock wave: the metallization threshold and ultrahigh defect densities," *Journal of Physics: Condensed Matter*, vol. 16, no. 46, pp. 8139–8153, nov 2004.

[23] H. Kishimura and H. Matsumoto, "Effect of phase transition in shock-recovered silicon," *Journal of Applied Physics*, vol. 103, no. 2, p. 023505, jan 2008.

[24] S. Sastry and C. Austen Angell, "Liquid-liquid phase transition in supercooled silicon." *Nature materials*, vol. 2, no. 11, pp. 739–43, nov 2003.

[25] C. Suryanarayana, "Mechanical alloying and milling," *Progress in Materials Science*, vol. 46, no. 1-2, pp. 1–184, jan 2001.

[26] M. Gamero-Castaño, A. Torrents, L. Valdevit, and J.-G. Zheng, "Pressure-Induced Amorphization in Silicon Caused by the Impact of Electrosprayed Nanodroplets," *Physical Review Letters*, vol. 105, no. 14, p. 145701, sep 2010.

[27] L. Davison, *Fundamentals of shock wave propagation in solids*. Springer, 2010.

[28] J. F. De La Mora and I. G. Loscertales, "The current emitted by highly conducting Taylor cones," *Journal of Fluid Mechanics*, vol. 260, no. -1, p. 155, feb 1994.

[29] M. Gamero-Castaño and J. F. de la Mora, "Direct measurement of ion evaporation kinetics from electrified liquid surfaces," *The Journal of Chemical Physics*, vol. 113, no. 2, p. 815, jun 2000.

[30] R. Borrajo-Pelaez, F. Saiz, and M. Gamero-Castaño, "The Effect of the Molecular Mass on the Sputtering of Si, SiC, Ge, and GaAs by Electrosprayed Nanodroplets at Impact Velocities up to 17 km/s," *Aerosol Science and Technology*, vol. 49, no. 4, pp. 256–266, 2015.

[31] F. Saiz and M. Gamero-Castaño, "Atomistic modeling of the sputtering of silicon by electrosprayed nanodroplets," *Journal of Applied Physics*, vol. 116, no. 5, pp. 1–7, 2014.

[32] M. O. Thompson, G. J. Galvin, J. W. Mayer, P. S. Peercy, J. M. Poate, D. C. Jacobson, A. G. Cullis, and N. G. Chew, "Melting Temperature and Explosive Crystallization of Amorphous Silicon during Pulsed Laser Irradiation," *Physical Review Letters*, vol. 52, no. 26, pp. 2360–2363, jun 1984.

[33] D. C. Swift, G. J. Ackland, A. Hauer, and G. A. Kyrala, "First-principles equations of state for simulations of shock waves in silicon," *Physical Review B*, vol. 64, no. 21, p. 214107, nov 2001.

[34] "Large-scale atomic/molecular massively parallel simulator (LAMMPS)." [Online]. Available: https://lammps.sandia.gov

[35] S. Plimpton, "Fast Parallel Algorithms for Short-Range Molecular Dynamics," *Journal of Computational Physics*, vol. 117, no. 1, pp. 1–19, mar 1995.

[36] H. J. C. Berendsen, J. P. M. Postma, W. F. van Gunsteren, A. DiNola, and J. R. Haak, "Molecular dynamics with coupling to an external bath," *The Journal of Chemical Physics*, vol. 81, no. 8, pp. 3684–3690, oct 1984.

[37] J. Samela, J. Kotakoski, K. Nordlund, and J. Keinonen, "A quantitative and comparative study of sputtering yields in Au," *Nuclear Instruments and Methods in Physics Research Section B: Beam Interactions with Materials and Atoms*, vol. 239, no. 4, pp. 331–346, oct 2005.

[38] R. Borrajo-Pelaez and M. Gamero-Castaño, "The effect of the molecular mass on the sputtering by electrosprayed nanodroplets," *Applied Surface Science*, vol. 344, pp. 163–170, 2015.

[39] "Winmostar." [Online]. Available: https://winmostar.com/en/

[40] B. D. Prince, P. Tiruppathi, R. J. Bemish, Y. H. Chiu, and E. J. Maginn, "Molecular Dynamics Simulations of 1-Ethyl-3-methylimidazolium Bis[(trifluoromethyl)sulfonyl]imide Clusters and Nanodrops," *Journal of Physical Chemistry A*, vol. 119, no. 2, pp. 352–368, 2015.

[41] L. Martínez, R. Andrade, E. G. Birgin, and J. M. Martínez, "PACKMOL: A package for building initial configurations for molecular dynamics simulations," *Journal of Computational Chemistry*, vol. 30, no. 13, pp. 2157–2164, oct 2009.

[42] J. N. Lopes and A. A. Pádua, "Molecular force field for ionic liquids composed of triflate or bistriflylimide anions," *Journal of Physical Chemistry B*, vol. 108, no. 43, pp. 16 893–16 898, 2004.

[43] C. Cadena, J. L. Anthony, J. K. Shah, T. I. Morrow, J. F. Brennecke, and E. J. Maginn, "Why is CO2 so Soluble in Imidazolium-Based Ionic Liquids?" *Journal of the American Chemical Society*, vol. 126, no. 16, pp. 5300–5308, 2004.

[44] Y.-R. Luo and Y.-R. Luo, *Comprehensive handbook of chemical bond energies*. CRC Press, 2007.

[45] "Ovito." [Online]. Available: https://www.ovito.org